RESEARCH ARTICLE

Sinking of Dense North Atlantic Waters in a Global Ocean Model: Location and Controls

C. A. Katsman[1] , S. S. Drijfhout[2,3,4], H. A. Dijkstra[3], and M. A. Spall[5]

[1]Department of Hydraulic Engineering, Delft University of Technology, Civil Engineering and Geosciences, Environmental Fluid Mechanics, Delft, Netherlands, [2]Royal Netherlands Meteorological Institute, De Bilt, the Netherlands, [3]Institute for Marine and Atmospheric Research Utrecht, Utrecht University, Utrecht, the Netherlands, [4]National Oceanography Centre Southampton, University of Southampton, Southampton, UK, [5]Woods Hole Oceanographic Institution, Woods Hole, MA, USA

Abstract We investigate the characteristics of the sinking of dense waters in the North Atlantic Ocean that constitute the downwelling limb of the Atlantic Meridional Overturning Circulation (AMOC) as simulated by two global ocean models: an eddy-permitting model at 1/4° resolution and its coarser 1° counterpart. In line with simple geostrophic considerations, it is shown that the sinking predominantly occurs in a narrow region close to the continental boundary in both model simulations. That is, the regions where convection is deepest do not coincide with regions where most dense waters sink. The amount of near-boundary sinking that occurs varies regionally. For the 1/4° resolution model, these variations are in quantitative agreement with a relation based on geostrophy and a thermodynamic balance between buoyancy loss and alongshore advection of density, which links the amount of sinking to changes in density along the edge of the North Atlantic Ocean. In the 1° model, the amount and location of sinking appears not to be governed by this simple relation, possibly due to the large impact of overflows and nonnegligible cross-shore density advection. If this poor representation of the processes governing the sinking of dense waters in the North Atlantic Ocean is a generic feature of such low-resolution models, the response of the AMOC to changes in climate simulated by this type of models needs to be evaluated with care.

1. Introduction

The Atlantic Meridional Overturning Circulation (AMOC) plays an important role in climate variability. The classical view of an "ocean conveyor belt" with northward surface currents and southward return currents in the North Atlantic Ocean transporting convectively formed dense waters to the other ocean basins (Broecker, 1991) suggests a tight relation between deep ocean convection and sinking. However, deep convection regions feature a large vertical heat and salt transport, but very little vertical mass transport (Marshall & Schott, 1999; Send & Marshall, 1995), as intense downwelling in convective plumes is balanced by upwelling in the surrounding areas.

Earlier studies have pointed out that it is unlikely that large-scale downwelling like that associated with the AMOC occurs in the ocean interior as vorticity conservation imposes strong constraints on the ocean circulation there (e.g., Brüggemann et al., 2017; Pedlosky, 2003; Scott & Marotzke, 2002; Spall, 2010; Spall & Pickart, 2001; Straneo, 2006). Instead, it has been argued that the net sinking of dense waters that constitute the downwelling limb of the AMOC must take place near continental boundaries. In the ocean interior, the dominant terms in the vorticity balance are the vortex stretching that arises from vertical motions ($f\partial w/\partial z$) and the meridional advection of planetary vorticity (βv). As a consequence, weak vertical motions in the geostrophic ocean interior are associated with (much stronger) horizontal motions (e.g., Rhines, 1986; Schott & Stommel, 1978). Scaling arguments show that this associated horizontal transport is an order of magnitude larger than the downwelling transport itself (Spall & Pickart, 2001, hereafter SP01). That is, to sustain the present-day AMOC by sinking in the interior, a horizontal circulation of roughly 150 Sv (1 Sv$=10^6$ m^3/s) would be required in the North Atlantic Ocean, which is obviously much stronger than what is observed.

Near boundaries and topography, the geostrophic constraints are lifted and a different vorticity balance can arise for which the stretching of planetary vorticity associated with the sinking is balanced by dissipation (Brüggemann et al., 2017; Spall, 2010). In regions that exhibit strong eddy activity (which are generally also

found near continental boundaries) nonlinear eddy fluxes of vorticity may play an important role in balancing the vortex stretching associated with the sinking as well (Brüggemann et al., 2017; Spall, 2004, 2008, 2010).

SP01 analyzed the dynamics of the downward transport near a continental boundary from a thermodynamic perspective. They considered a flow along a straight continental boundary, with a deep mixed layer near the coast resulting from cooling by the atmosphere. In the absence of diffusion, the thermodynamic balance within this mixed layer is between horizontal advection of density and the densification of the water in the alongshore direction induced by the surface cooling. SP01 showed that this yields a horizontal circulation in thermal wind balance with the density gradient that spirals counterclockwise with depth. Analogous to the mechanism of an Ekman spiral, such a cooling spiral induces strong vertical motions when the cooling occurs near a coast because of mass conservation, in a thin ageostrophic boundary layer (Schott & Stommel, 1978, SP01). Details of such a thermal boundary layer were studied by Pedlosky and Spall (2005), who showed that a cell-like structure emerges with strong sinking near the coast accompanied by weaker upwelling just offshore.

Straneo (2006) proposed an elegant two-layer model illustrating the dynamics of a flow along a boundary subject to buoyancy loss and the associated downward transport. The model consists of a buoyant boundary current and a denser interior, representing the Irminger Current and the convection region in the Labrador Sea. In this model, the boundary current is partly baroclinically driven due to the difference in thickness of the denser water layer between the interior and the boundary current. She showed that when the boundary current loses buoyancy along the perimeter of the marginal sea, either by atmospheric cooling or through lateral eddy fluxes, downward transport has to occur in the boundary current. As the boundary current becomes denser along its route (i.e., the upper layer becomes thinner), a cross-shore baroclinic flow toward the boundary develops. Due to mass conservation, this yields downward motions in a thin (unresolved) boundary layer when it impinges on the coast.

The above considerations imply that the regions where most of the sinking occurs (the steep continental slopes of the North Atlantic Ocean) do not coincide with the regions where convection reaches deepest (the interior of its marginal seas). So far, highly idealized regional model studies (Brüggemann et al., 2017; Pedlosky & Spall, 2005; Spall, 2004, 2010, 2011) and laboratory experiments (Cenedese, 2012) have confirmed that sinking motions indeed predominantly occur in a narrow region adjacent to the boundary. However, it is unclear if this is also the case in the current generation of global ocean models, and in particular for the climate models that are used to project possible changes in the AMOC over this century (Collins et al., 2013). The highly diffusive nature of such coarse resolution models may affect the sinking, in case the dissipation of vorticity already breaks the geostrophic vorticity balance at mid-ocean rather than only near the continental boundaries. As a possible consequence, the response of such a diffusive model to changes in environmental conditions (oceanic and atmospheric warming, freshwater forcing) may be misrepresented. In this study, we address this question by characterizing the sinking motions associated with the downwelling limb of the AMOC in a global ocean model, contrasting two simulations with differing horizontal resolution (1° and 1/4° grid spacing).

The study by SP01 highlighted the role of the ocean properties in controlling the amount of sinking that occurs near a boundary in a region subject to buoyancy loss. They derived a quantitative relation for the meridional overturning W_B as a function of the alongshore density change $\Delta\rho_B$ (their equation (7)):

$$W_B = \frac{g\Delta\rho_B \, z_{sink}^2}{2\rho_0 f},$$

(1)

with f the Coriolis parameter, g the gravitational acceleration, ρ_0 a reference density, and z_{sink} the depth at which the downward mass transport is at its maximum. Equation (1) emphasizes that local processes in marginal seas can exert control on AMOC variations: all processes yielding a local density change (atmospheric cooling, but also diffusion and lateral eddy fluxes for example) affect $\Delta\rho_B$ and hence the amount of sinking that occurs locally near a continental boundary. In this study, we test whether this relation holds in the complex global ocean models analyzed here and predicts the amount of near-boundary sinking that occurs in the North Atlantic Ocean. One important difference with the idealized models used by SP01 and Straneo (2006) is the fact that the North Atlantic is not a closed basin and exchanges with the Nordic Seas

and Arctic Ocean are possible via the Iceland-Scotland Ridge, Denmark Strait, and Davis Strait. The vertical transport associated with the overflows is not taken into account in equation (1). Moreover, SP01 derived the relation for the situation that a mixed layer of depth h_{mld} is present along the coast, and that the strength of the overturning peaks at a depth at the middle of this mixed layer ($z_{sink} = h_{mld}/2$). It will be shown that in the model simulations that are analyzed here, mixed layers near the coast are much shallower than the depth at which the overturning peaks.

The two hindcast simulations are introduced in section 2. Next, the downwelling limb of the AMOC is characterized by means of the vertical velocity (section 3) and the vertical transport at the depth where the AMOC strength peaks (section 4). In section 5, we distinguish near-boundary sinking from sinking in the interior, and analyze the sinking on a path along the northern edge of the North Atlantic Ocean to test whether equation (1) is valid for the two global simulations. A summary and discussion (section 6) concludes this study.

2. Hindcast Simulations

We analyze the sinking of dense waters in two hindcast simulations performed with the NEMO/OPA z coordinate model, at a resolution typical for state-of-the-art coupled climate models (Collins et al., 2013; Haarsma et al., 2016). The first hindcast (hereafter referred to as ORCA025) is the global ocean/sea-ice simulation performed by the DRAKKAR Group, at an eddy-permitting resolution of 1/4°. The setup is identical to that of the simulation described in detail in Barnier et al. (2006) and Penduff et al. (2010), except that no salinity restoring under sea ice is applied. The second hindcast (referred to as ORCA1) is an uncoupled simulation performed with the ocean component of the global climate model EC-EARTH, at a coarser horizontal resolution of 1°. An extensive description of this ocean model configuration can be found in Sterl et al. (2012, section 2.3).

In both model simulations, a C-grid is applied in a tripolar configuration with poles in Siberia, Canada, and at the South Pole. To define the bathymetry, the ETOPO2 bathymetry of NGDC (National Geophysical Data Center) is applied, smoothed to match the appropriate model grid. Bottom topography is represented by partial steps (Adcroft et al., 1997).

The main differences between the models are in the formulation of the dissipation and of the diffusion of tracers. In the horizontal momentum equations, ORCA025 uses a biharmonic viscosity formulation with a coefficient that depends on grid size, while ORCA1 uses a constant Laplacian eddy viscosity parameterization (Table 1). The horizontal diffusion of tracers is represented by a Laplacian operator in both configurations, but with different coefficients (Table 1). In the vertical, the Turbulent Kinetic Energy (TKE) parameterization (Blanke & Delecluse, 1993) is applied, which parameterizes ocean convection arising from static instability of the water column by an enhancement of both the vertical viscosity and diffusivity.

Both versions of the model are forced by prescribed atmospheric conditions. Atmospheric temperature, humidity, and wind stress are derived from the ERA40 reanalysis (Uppala et al., 2005), radiative fluxes, and precipitation are extracted from the Coordinated Ocean and Sea-Ice Reference Experiments forcing data set

Table 1
Key Model Parameters Applied in the ORCA025 and ORCA1 Hindcast Simulations

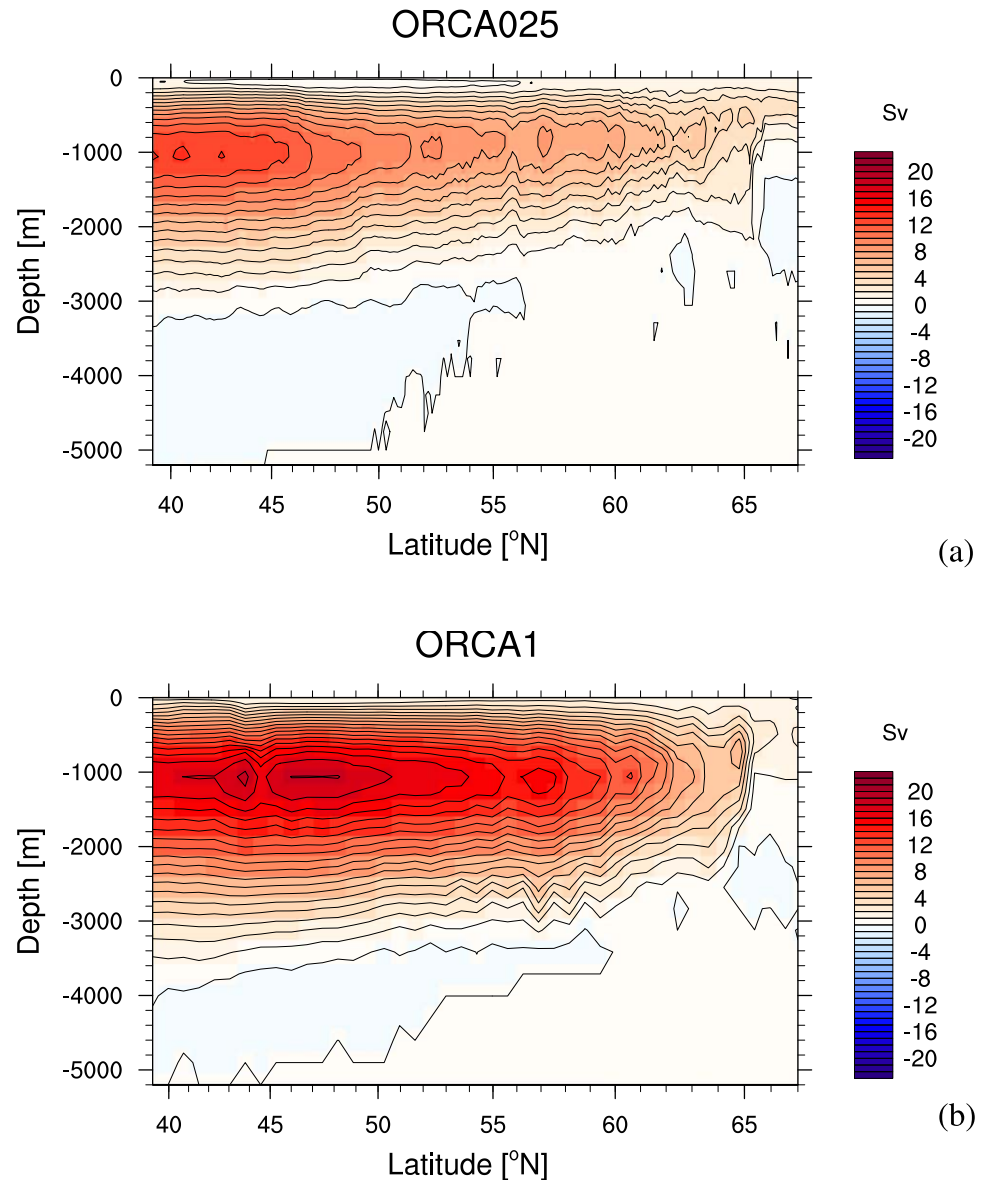|	ORCA025	ORCA1
Horizontal resolution	1/4°×1/4°, 1,442 × 1,021 grid points	1°×1°, 362 × 292 grid points
Vertical resolution	46 vertical levels, thickness 6–250 m	42 vertical levels, thickness 10–300 m
Horizontal viscosity	At equator: -1.5×10^{11} m^4 s^{-1}, decreasing poleward $\propto$ (grid size)^3	1.0×10^4 m^2 s^{-1}
Horizontal diffusivity	At equator: 3.0×10^2 m^2 s^{-1}, decreasing poleward $\propto$ grid size	1.0×10^3 m^2 s^{-1}
TKE parameterization		
Background	1.0×10^{-5} m^2 s^{-1}	1.0×10^{-5} m^2 s^{-1}
In case of static instability	Up to 10 m^2 s^{-1}	Up to 10 m^2 s^{-1}

Note. See Barnier et al. (2006) and Sterl et al. (2012), respectively, for more details on the model setup.

(Large & Yeager, 2004). Bulk formula are used to compute the required surface boundary conditions from these atmospheric data (Timmermann et al., 2005). Initial temperature and salinity datasets are based on the climatological fields from the World Ocean Database (Levitus, 1998).

Both hindcast simulations cover the entire ERA-40 period from 1958 to 2001, and all analyses shown in this paper are for the 44 year mean circulation.

3. Vertical Velocity

The AMOC circulation in ORCA025 and ORCA1 is shown in Figure 1 by means of the stream function in the latitude-depth plane, computed as the longitudinal integral of the meridional velocity field of the two hind-casts. The AMOC in ORCA025 is weaker than in ORCA1, with a maximum overturning of 13.1 Sv versus 18.3 Sv (1 Sv $= 10^6$ m^3/s). It is also shallower than in ORCA1, and its maximum is located slightly farther south (40.6°N versus 43.8°N). For both simulations, a weak reverse cell is present below 3,000 m. Such differences

Figure 1. Time-mean Atlantic Meridional Overturning Circulation (AMOC) in the (a) ORCA025 and (b) ORCA1 hindcasts (in Sv, 1 Sv $= 10^6$ m^3/s).
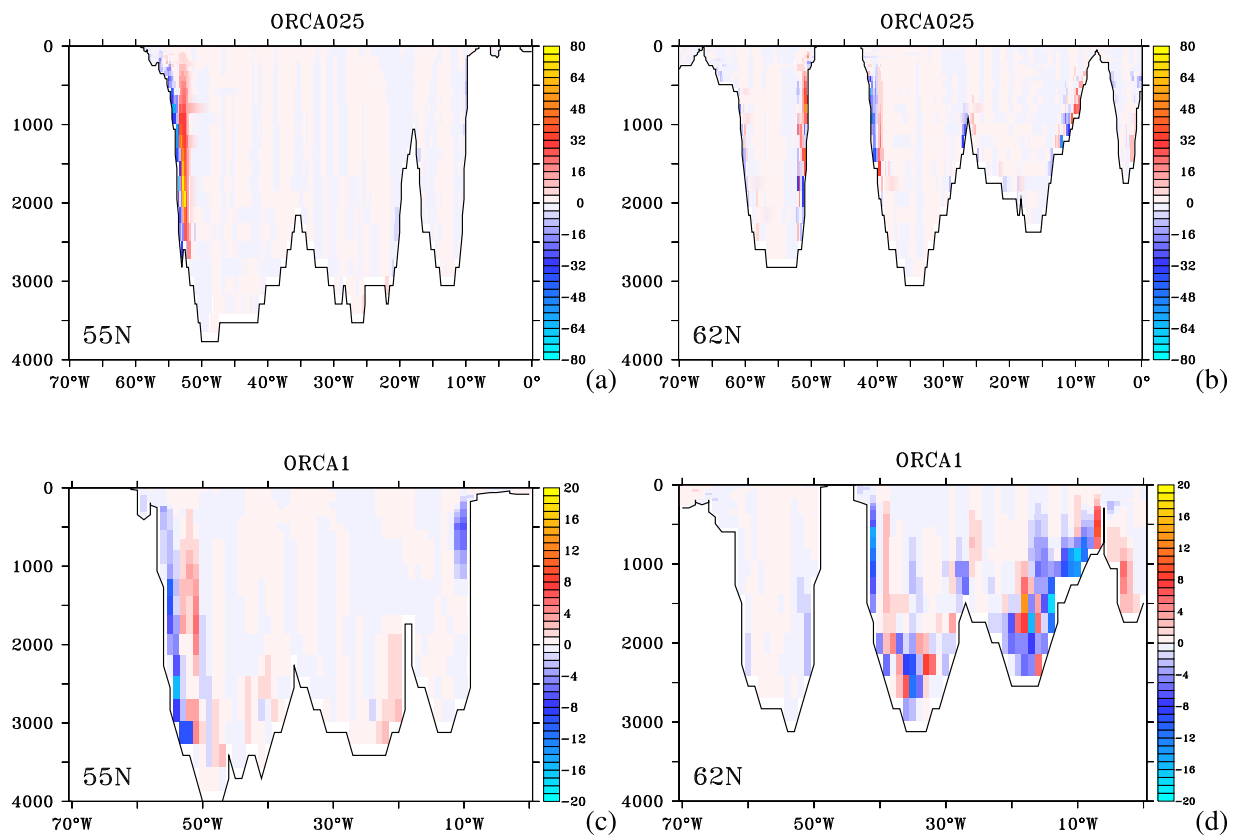
Figure 2. Zonal sections of the vertical velocity at (left) 55°N and (right) 62°N, for (a and b) ORCA025 and (c and d) ORCA1 (in m/d, note the difference in color scale between (a and b) and (c and d)).

are within the ranges seen in various climate model simulations at comparable resolution (e.g., Cheng et al., 2013; Danabasoglu et al., 2014; Wang et al., 2014).

However, a zonally integrated overturning stream function does not reveal where in the North Atlantic basin the sinking associated with the AMOC actually takes place. When the vertical motions are analyzed, strong downward velocities are seen on the continental slopes, while velocities are generally much weaker in the interior (Figure 2). At several locations, the downward motion is accompanied by upward motion slightly farther offshore (e.g., western boundary of the Labrador Sea at 55°N—Figures 2a–2c; western boundary of the Irminger Sea at 62°N—Figures 2b–2d). This boundary layer structure is also seen in the idealized model simulations by Spall (2010). Such a downwelling and upwelling structure is expected from boundary layer theory (Pedlosky, 2003; Pedlosky & Spall, 2005). In addition to these cell-like structures, ORCA1 also displays strong vertical motions in the deep interior (Figure 2d), below 2,000 m. Their location and depth suggest that these strong vertical motions are related to the deep overflows, which are presumably not correctly represented at this resolution (Winton et al., 1998). As a consequence, maps of the vertical velocity minimum found in the water column (largest sinking) display a clear separation between regions where large downward velocities occur and quiet regions for ORCA025 (Figure 3a), while such a clear separation is absent in ORCA1 (Figure 3b). The same picture emerges from the accompanying maxima in vertical velocity (Figures 3c and 3d). In summary, this analysis of the vertical velocity field confirms that indeed most of the sinking that constitutes the downwelling limb of the AMOC occurs on the continental slopes, and not in the (geostrophic) ocean interior.

4. Vertical Transport at the Depth of the AMOC Maximum

Next, we explore the downwelling limb of the AMOC in more detail, focusing on the vertical velocity at the depth at which the basin-integrated sinking of dense waters in the North Atlantic Ocean is at its maximum
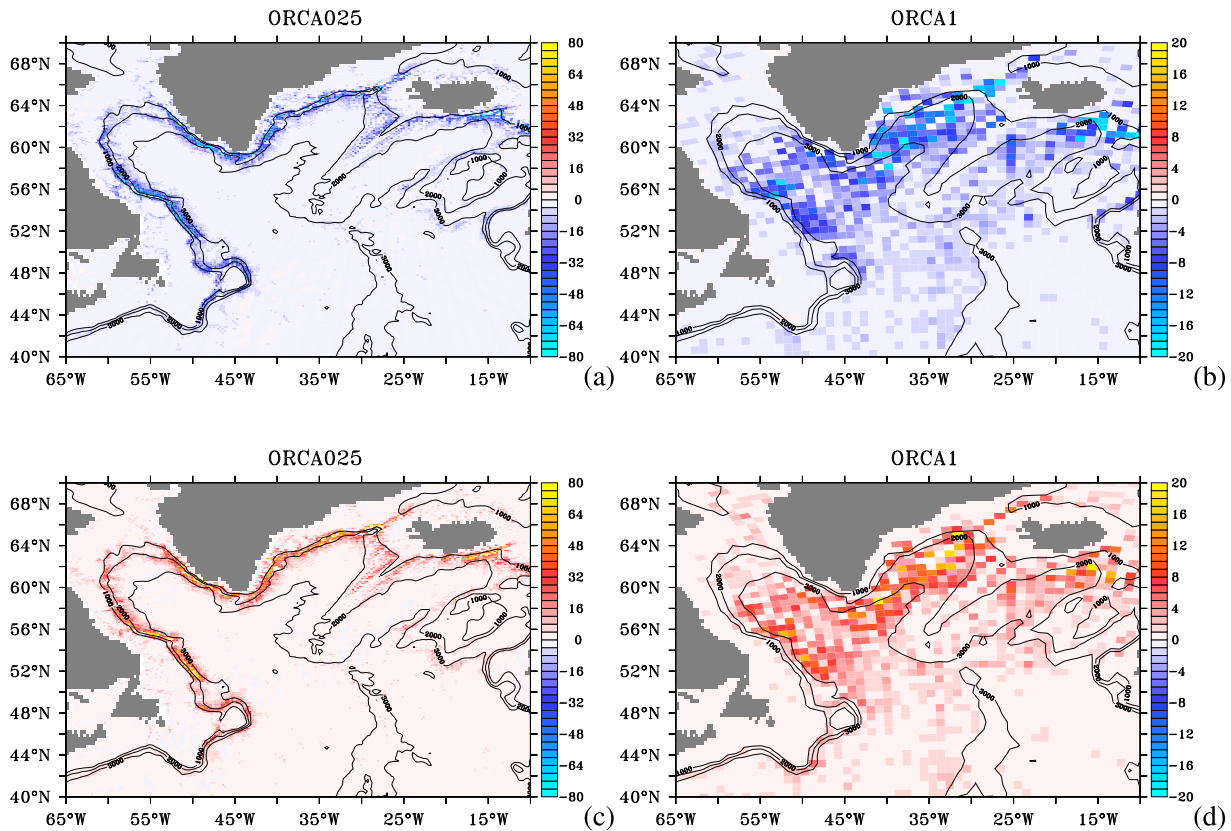
Figure 3. (a and b) Minimum in vertical velocity found in the water column, for (a) ORCA025 and (b) ORCA1; (c and d) as (a and b), but for the maximum (velocities in m/d, note the factor four difference in color scale between the ORCA025 and ORCA1 case).

(Figures 4a and 4b). This depth (which we refer to as $z=z_{sink}$) appears to be virtually the same in the two hindcast simulations: $z_{sink}=1,061$ m for ORCA025 and $z_{sink}=1,062$ m for ORCA1. Integrated over the domain 40°N–67°N × 65°W–5°W, there is a net sinking of 13.3 Sv in ORCA025, and of 17.3 Sv in ORCA1 (Table 2). These numbers differ slightly from the maximum AMOC transports that were found in the previous section (13.1 Sv and 18.3 Sv, respectively), due to exchange between the Atlantic Ocean and the Arctic Ocean at various depths. Although the overturning stream function in ORCA1 shows little net transport across 65N, this is somewhat misleading because there is compensating exchange across the Greenland-Scotland Ridge. As discussed further below, the low resolution model does produce a dense overflow through Denmark Strait. Note that the regions where the mixed layer depth peaks in winter (green contours in Figure 4) do not coincide with regions of strong sinking (Scott & Marotzke, 2002). This is particularly clear for the ORCA025 configuration.

Large variations in sinking exist on the scale of the marginal seas. To illustrate this, we subdivide the North Atlantic domain in six regions: (1) Denmark Strait, (2) the Labrador Sea, (3) the Irminger Sea, (4) the Iceland Basin (excluding the overflows between Iceland and Scotland), (5) the Iceland-Scotland Ridge, and (6) the Atlantic Ocean between 40°N and 48°N (Figure 4 and Table 2).

The overflow regions (1) and (5) carry a substantial part of the sinking (4.8 Sv in ORCA025 and 8.7 Sv in ORCA1), amounting to 36% and 50% of the total sinking, respectively (Table 2). The Denmark Strait overflow region contributes slightly less than the overflows on the Iceland-Scotland Ridge in both simulations. The remainder of the sinking (8.5 Sv for ORCA025 and 8.6 Sv for ORCA1) occurs in (2) the Labrador Sea, (3) the Irminger Sea, and (4) the Iceland Basin. For ORCA025, the contribution from the Iceland Basin is as large as the contributions from the Labrador and Irminger Seas combined, while in ORCA1 all three regions contain a similar contribution. Only in ORCA025 there is substantial sinking south of 48°N (region (6), 21%), while in ORCA1 this region displays weak upwelling. Notably, the patterns of vertical motion are highly irregular, with substantial sinking and strong upwelling often occurring in adjacent grid boxes, even for the 44 year
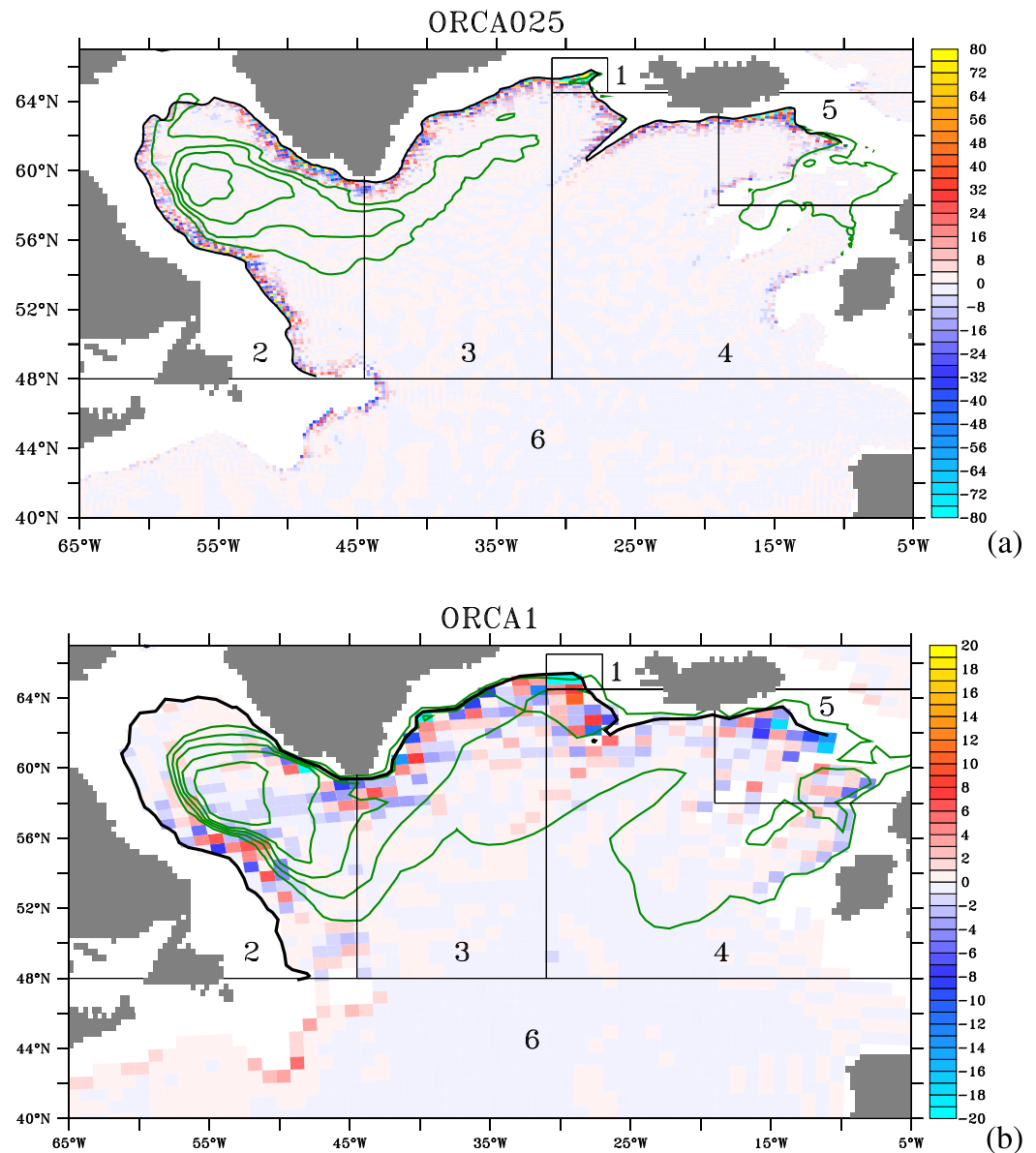
Figure 4. Vertical velocity per grid box at depth z_{sink} in (a) ORCA025 and (b) ORCA1 (in m/d). Blue colors denote sinking, red colors denote upwelling; note the factor four difference in color scale between the two plots. Vertical motions in grid boxes containing overflows (regions 1 and 5) exceed the chosen color scale. Green contours outline the time-average of the maximum mixed layer depth (contour interval is 500 m; maximum is 2,255 m for ORCA025 and 2,882 m for ORCA1), the thick black solid line is the $z = z_{sink}$ isobath. The net vertical transport over each of the six regions is provided in Table 2.

mean displayed here. This is an effect of the rough bathymetry, which locally forces upward and downward flows. However, the net vertical motion in all regions along the edge of the North Atlantic Ocean is downward (Table 2). The only marginal sea for which observation-based estimates of the local sinking are available is the Labrador Sea, from analyses of hydrographic data (Pickart & Spall, 2007) and of Argo floats (Holte & Straneo, 2017). Both studies report a sinking of 1–2 Sv, which compares favorably with what is found in the ORCA025 simulation.

5. Sinking Along the Edge of the North Atlantic Ocean

It is expected that sinking can occur in regions where the circulation has a substantial ageostrophic component, so that a nongeostrophic vorticity balance can be reached (section 1). In a noneddying flow, this is

Table 2

Characteristics of the Sinking Associated With the Downwelling Limb of the AMOC in the ORCA025 and ORCA1 Hindcast Simulations (in Sv)

	ORCA025	ORCA1
Maximum AMOC transport	13.1	18.3
Vertical transport integrated over 40°N–67°N x 67°W–5°W	−13.3	−17.3
Vertical Transport Integrated by Region		
1. Denmark Strait	−2.2 (17%)	−4.7 (27%)
2. Labrador Sea	−1.4 (11%)	−3.4 (20%)
3. Irminger Sea	−1.4 (11%)	−4.0 (23%)
4. Iceland Basin	−2.9 (22%)	−2.0 (12%)
5. Iceland-Scotland Ridge	−2.6 (19%)	−4.0 (23%)
6. 40°N–48°N	−2.8 (21%)	+0.9 (5%)

Note. Regions 1–6 are defined in Figure 4, % are given with respect to the total vertical transport at $z = z_{sink}$.

expected to occur in a boundary region where friction becomes important. To calculate how much sinking occurs in this boundary region with respect to the ocean interior we make use of the characteristics of the subpolar gyre, reflected in the barotropic stream function (Figures 5a and 5b). ORCA025 displays a stronger subpolar gyre circulation than ORCA1 (−40.8 Sv in ORCA025 and −28.8 Sv in ORCA1), a narrower boundary current and a more pronounced western intensification of the gyre.

By calculating the integrated vertical transport at $z = z_{sink}$ over all grid boxes for which the associated value of the barotropic stream function falls within a specified interval, we obtain the vertical transport distinguished by streamline interval (Figures 5c–5e). Both model simulations display a striking change in behavior when moving from the coast toward the interior of the subpolar gyre: strong net downward motion is found only in the regions that coincide with values of the
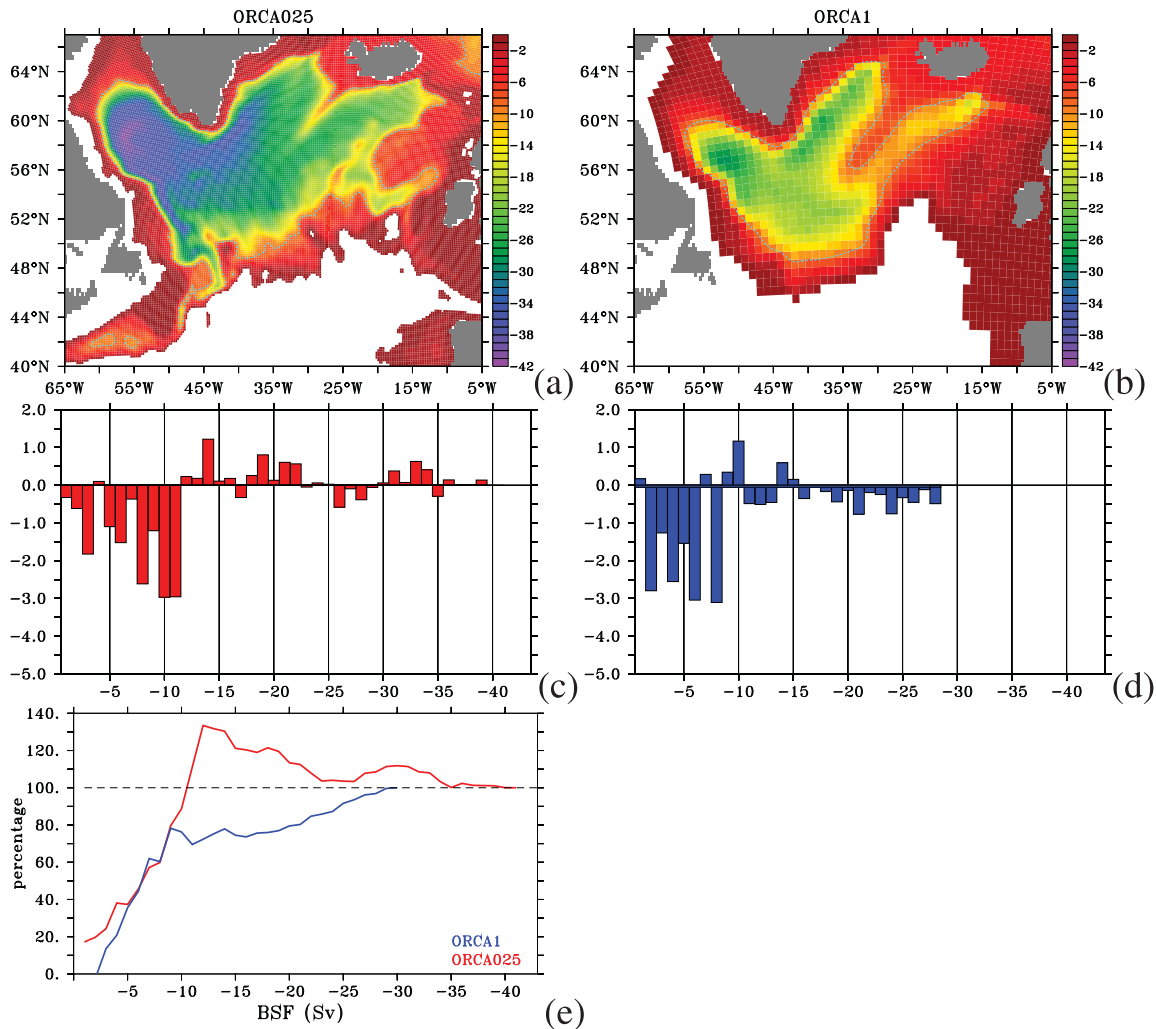
Figure 5. (a and b) Barotropic stream function of the subpolar gyre (in Sv) averaged over 1958–2001, in (a) ORCA025 and (b) ORCA1 (positive values, corresponding to the anticyclonic subtropical gyre, have been masked); 80% of the sinking occurs between the coast and the −9 Sv contour line (dashed, lightblue). (c and d) integrated vertical transport at depth $z = z_{sink}$ over all grid boxes within 1 Sv intervals of barotropic stream function values, in (c) ORCA025 and (d) ORCA1; (e) cumulative vertical transport as a function of barotropic stream function streamline interval, normalized by the net sinking over the entire displayed domain 40°N–67°N × 65°W–5°W.
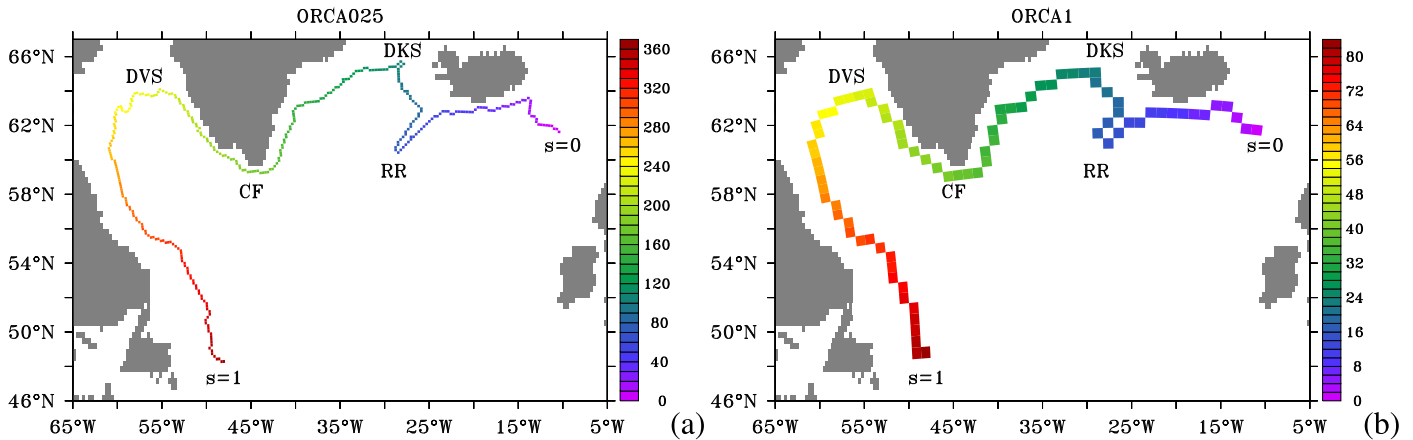
Figure 6. (a and b) Map of the path along the $z=z_{sink}$ isobath for (a) ORCA025 and (b) ORCA1. The alongshore coordinate $s \equiv 0$ near Faroe-Scotland Ridge at 10°W, $s \equiv 1$ is on the Labrador coast at 48°N. Note that it is defined as the grid point closest to the coast that has a value for w at depth $z=z_{sink}$. In regions with steep topography, this grid point is not necessarily the grid point nearest to the bottom. The entire path $s \in [0, 1]$ consists of 361 grid points for ORCA025 and 82 grid points for ORCA1 (color coded). Key locations annotated in the plot are Reykjanes Ridge (RR, $s \simeq 0.19$), Denmark Strait (DKS, $s \simeq 0.28$), Cape Farewell (CF, $s \simeq 0.48$), and Davis Strait (DVS, $s \simeq 0.65$).

barotropic stream function close to zero, i.e., at locations close to the coast where the boundary current of the subpolar gyre is found. As much as 80% of the net sinking at the depth $z=z_{sink}$ occurs between the coast and the 0 Sv and -9 Sv contourlines of the barotropic stream function for both ORCA1 and ORCA025. As the viscosity in the ORCA1 hindcast simulation is much higher than in ORCA025 (Table 1), the width of this near-boundary region where sinking occurs covers a much larger area in ORCA1. Farther away from the coast, the results for the two model simulations differ: while ORCA025 displays slight upwelling oceanward from the -11 Sv streamline (Figures 5c–5e), ORCA1 displays net sinking over the gyre interior as well (Figures 5d and 5e). This analysis confirms the tight link between the region where friction plays a role and regions where sinking occurs. The notion that the sinking region coincides with the boundary current region of the subpolar gyre is in line with the idealized models proposed by Spall (2004) and Straneo (2006).

Next, we define a path along the northern edge of the North Atlantic Ocean along the $z=z_{sink}$ isobath for ORCA025 and ORCA1 (one grid point wide, Figures 6a and 6b), to analyze the near-boundary sinking and its relation to the alongshore density variations (section 1). The alongshore coordinate $s \equiv 0$ near Iceland-Scotland Ridge at 10°W, $s \equiv 1$ is on the Labrador coast at 48°N. The vertical transport w_T along this path is
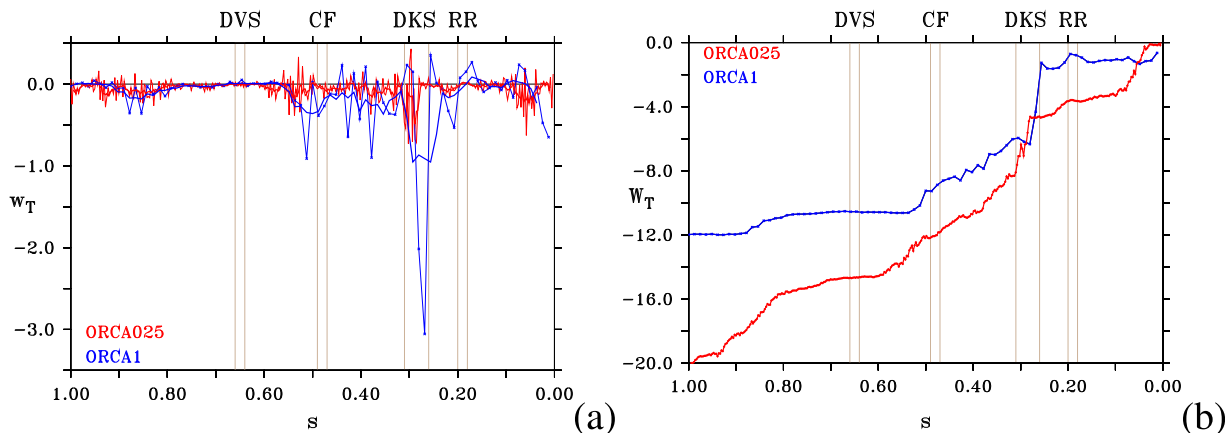

Figure 7. (a) Vertical transport $w_T(s)=w(s)\Delta x_s \Delta y_s$ and (b) cumulative vertical transport $W_T(s)=\sum_0^s w_T(s)$ along the edge of the North Atlantic Ocean at depth $z=z_{sink}$, for (red) ORCA025 and (blue) ORCA1 (in Sv, thin line: all grid points; thick line: five-point smoothed). Key locations along the path are labeled (see Figure 6). The horizontal axis has been flipped to better match the longitudes of the path locations ($s = 0$ near Faroe-Scotland Ridge at 10°W, $s = 1$ is on the Labrador coast at 48°N). Note that the values displayed in Figure 7a are not necessarily the near-bottom vertical velocities: in regions where the continental slope is steep, grid points with nonzero vertical velocities may exist below the depth level $z=z_{sink}$.

highly variable for both configurations, with the largest values occurring in the Denmark Strait Overflow region (DKS, Figure 7a). The cumulative transport (Figure 7b) reveals that a surprising amount of sinking takes place along this narrow path: the net vertical transport $W_T(s=1)$ is -20.2 Sv for ORCA025 and -12.0 Sv for ORCA1. Note that for ORCA025, the downward transport on this narrow path is much larger than the basin-integrated downwelling of 13.3 Sv (Table 2). This is a consequence of the cell-like boundary layer structure seen in Figure 2: the narrow path mostly contains the downwelling part of the cells. The Davis Strait region ($s=0.6-0.8$, DVS) is a region where hardly any sinking occurs in either of the simulations. In fact, in ORCA1 there is very little sinking east of Denmark Strait (DKS) or west of Cape Farewell (CF), and essentially all the near-boundary sinking occurs at Denmark Strait and closely downstream of it. There is 7.6 Sv of sinking between Denmark Strait (which is resolved by only two grid boxes in ORCA1, at $s=0.27-0.28$) and Cape Farewell ($s=0.48$), representing 63% of the total of 12.0 Sv of near-boundary sinking. In ORCA025, 37% of the total of 20.2 Sv of near-boundary sinking occurs along the same segment of the path.

According to the studies by SP01 and Straneo (2006), a key parameter governing this sinking adjacent to the coast is the alongshore density change. For ORCA025, the density increases over almost the entire depth range $z=0$ to $z=z_{sink}$ (Figures 8a–8c). The density at middepths increases sharply at $s=0.3$, where the overflow waters from Denmark Strait are entrained. For $s \geq 0.4$, the density near the surface decreases
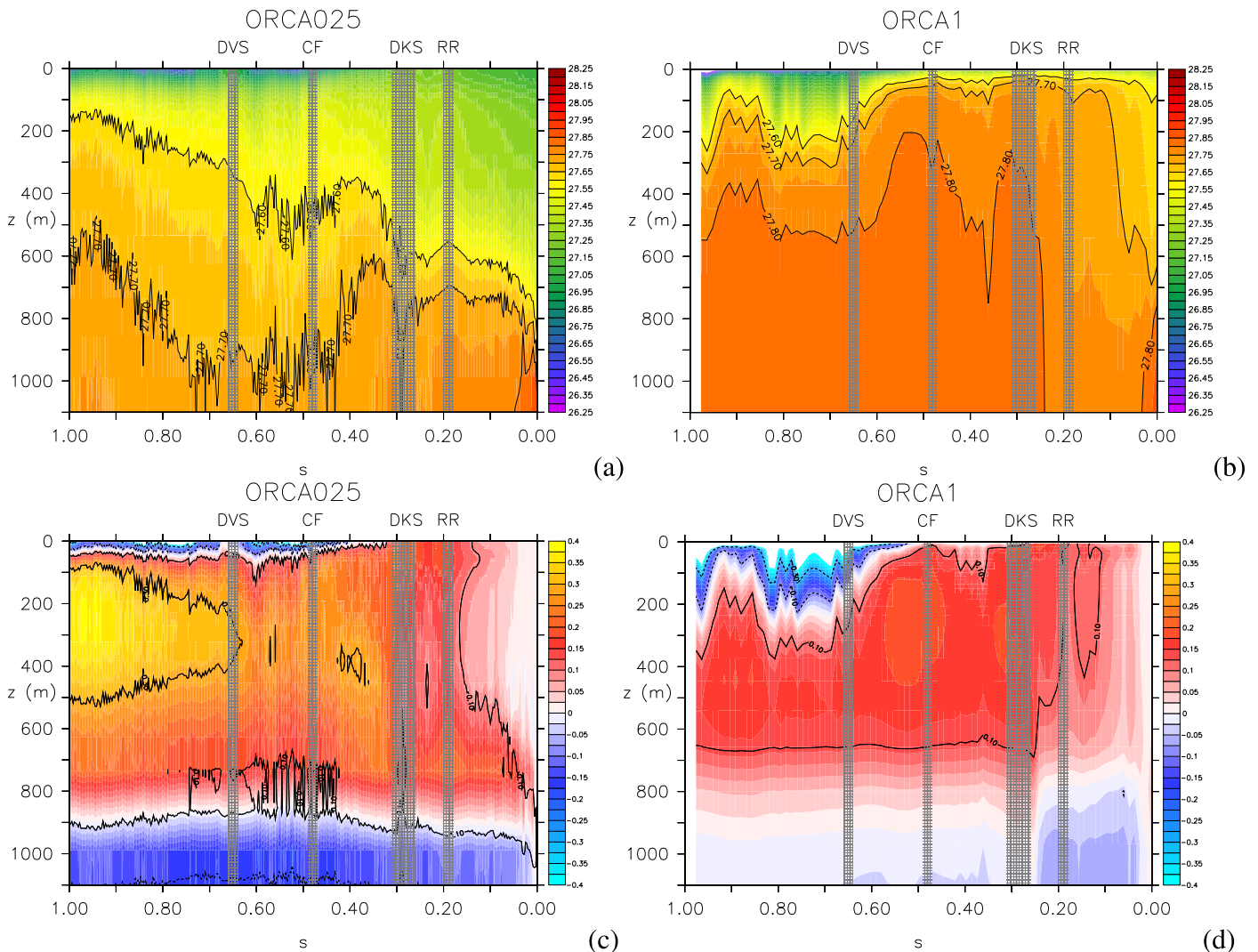
Figure 8. (a and b) Density $\sigma(s,z)=\rho(s,z)-1000$ for (a) ORCA025 and (b) ORCA1 (in kg/m^3). The $\sigma=27.6, 27.7$ and 27.8 kg/m^3 isopycnals are contoured; (c and d) density difference $\Delta\rho_B(s,z)=\rho(s,z)-\rho(0,z)$ as a function of the normalized alongshore coordinate s, for (c) ORCA025 and (d) ORCA1. Note that the horizontal axis has been flipped, key locations are annotated: RR = Reykjanes Ridge, DKS = Denmark Strait, CF = Cape Farewell, and DVS = Davis Strait (see also Figure 6).
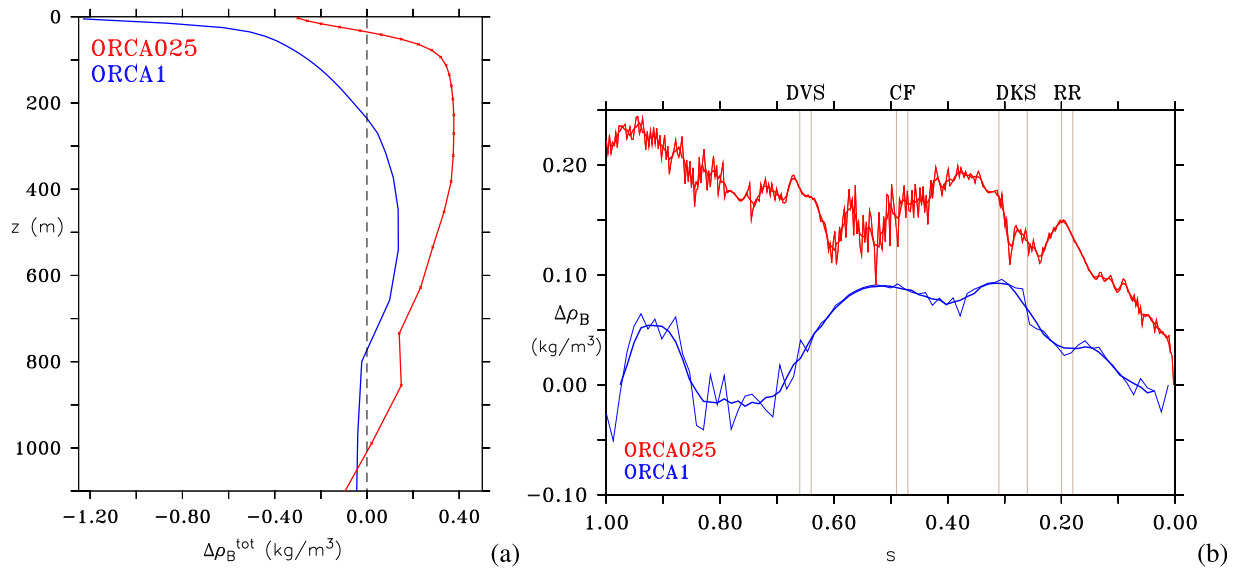
Figure 9. (a) Total density difference $\Delta\rho_B^{tot}(z) = \rho(1,z) - \rho(0,z)$ along the $z = z_{sink}$ isobath, for (red) ORCA025 and (blue) ORCA1; (b) depth-weighted density difference $\Delta\overline{\rho_B}(s) = \int_0^{z_{sink}} \rho_B(s,z)dz/z_{sink}$, as a function of the alongshore coordinate s, for (red) ORCA025 and (blue) ORCA1 (thin line: all grid points; thick line: five-point smoothed). Note that the horizontal axis has been flipped, key locations are annotated are RR = Reykjanes Ridge, DKS = Denmark Strait, CF = Cape Farewell, and DVS = Davis Strait (see Figure 6).

(Figure 8c). Here buoyant waters from the West Greenland Current and from Davis Strait mix with the waters farther offshore. However, below $z = 100$ m the density continues to increase past Davis Strait. The rising of the $\sigma = 27.6$ kg/m^3 isopycnal (Figure 8a) shows a striking resemblance to the highly idealized two-layer model proposed by Straneo (2006) to describe the characteristics of convection and sinking in the Labrador Sea and its relation to alongshore density changes (her Figure 1). Along the entire path, there is a net increase in density in ORCA025 over a depth range 50–1,000 m (red line in Figure 9a).

The results for ORCA1 are not in line with the theoretical considerations outlined in SP01 and Straneo (2006) or in observations within the Labrador Sea (Pickart & Spall, 2007): the density hardly increases along the path in this simulation (Figures 8b–8d). A striking feature is the strong decrease in density associated with buoyant waters entrained from the shelf ($s \geq 0.6$). These buoyant waters, which in this case predominantly enter via Davis Strait (DVS), have an impact at much larger depths than for ORCA025 and oppose the weak increase in density that is seen at larger depths. As a consequence, there is only a weak densification of the waters along the path (a factor two smaller than in ORCA025), and only over a limited depth range of 200–800 m (blue line in Figure 9a).

Finally, we test the quantitative relation between the near-boundary sinking and the alongshore density change proposed by SP01 (equation (1) and section 1). The sinking along the path was defined earlier as W_T (Figure 7b). In contrast to the situation considered by SP01 (with a mixed layer along the coast with a depth larger than $z = z_{sink}$), for this case the alongshore density change varies with depth (Figure 8). As the measure of the alongshore density change $\Delta\rho_B$ we use the depth-weighted density change $\Delta\overline{\rho_B}$ (Figure 9b), to take into account hydrostatic pressure variations in the entire water column above $z = z_{sink}$. This figure illustrates once more that only ORCA025 shows a clear densification in alongshore direction. For ORCA1, $\Delta\overline{\rho_B}(s)$ rises until Denmark Strait (DKS), and then decreases toward Davis Strait. Between Davis Strait and the end of the path $\Delta\overline{\rho_B}(s)$ oscillates around zero.

For ORCA025, there is a clear dependence of the sinking $W_T(s)$ on the alongshore density change $\Delta\overline{\rho_B}$ (circles in Figure 10). In fact, the slope of the scatter plot approaches that of the dashed lines denoting the theoretical dependence of $W_T(s)$ on $\Delta\overline{\rho_B}(s)$ from the start of the path past Reykjanes Ridge (RR) and from downstream of Cape Farewell (CF) to the end of the path. The largest deviations are seen at grid points between Denmark Strait overflow (DKS) and Cape Farewell (CF). There, the relation is not expected to hold as the sinking associated with overflows is governed by dynamics not taken into consideration in the derivation of equation (1). For ORCA1 (crosses in Figure 10), the relation between $W_T(s)$ and $\Delta\overline{\rho_B}(s)$ is in
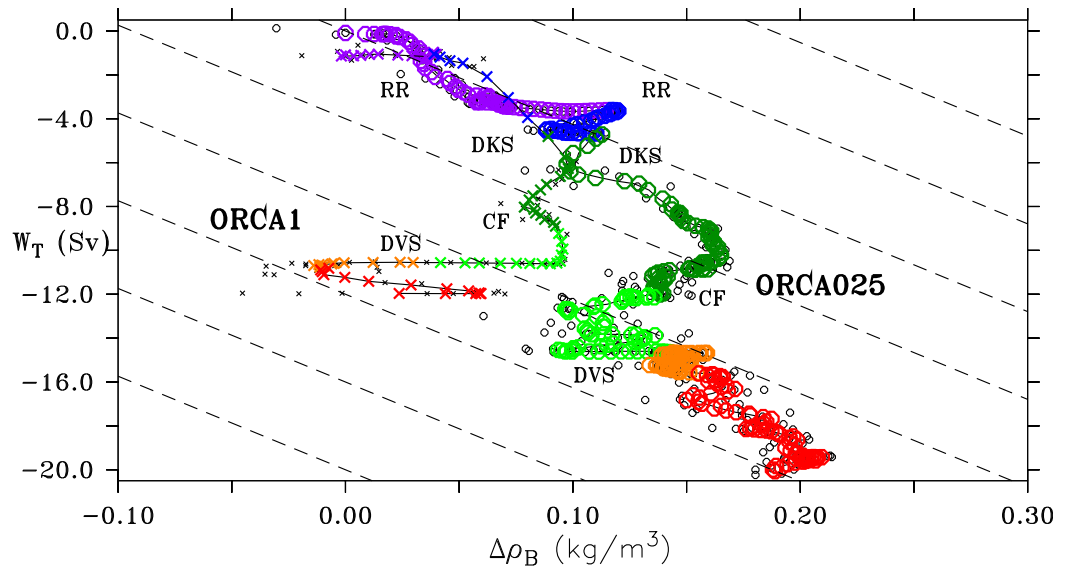
Figure 10. Scatterplot of the alongshore density difference $\Delta\overline{\rho_B}$ (in kg/m³) and the cumulative vertical transport W_T (in Sv), for (circles) ORCA025 and (crosses) ORCA1 along the path outlined in Figure 6 (black symbols: data for each grid point, colored symbols: five-point smoothed values). Key locations are labeled, the color coding indicates the path segment in accordance with Figure 6 (purple: start-RR, blue: RR-DKS, dark green: DKS-CF, light green: CF-DVS, orange: DVS-western Labrador Sea, red: western Labrador Sea-end). Dashed lines indicate the theoretical slope $gz_{sink}^2/2\rho_0 f$ that follows from equation (1).

reasonable agreement with the theoretical predictions by SP01 upstream of Denmark Strait only. Beyond that point, it comes at no surprise after assessing a lack of densification along the coast for ORCA1 (Figure 9b) that for this case the relation no longer holds. Changing the definition of $\Delta\overline{\rho_B}$ to the alongshore density difference averaged over depths $z=400$ m to $z=z_{sink}$ to exclude the impacts of the buoyant waters seen at $s>0.6$ (Figures 8b–8d) does not improve the results for ORCA1 (not shown). So while for ORCA025 the relation between sinking and density is in agreement with the theoretical estimate, except in regions where the overflows play a role, apparently the sinking that occurs on the continental slope in ORCA1 downstream of Denmark Strait is not well predicted by the variations in the alongshore density.

6. Summary and Discussion

We have presented an extensive analysis of the sinking associated with the Atlantic Meridional Overturning Circulation in a 1/4° and a 1° resolution global ocean model (referred to as ORCA025 and ORCA1, respectively). It was shown that the deep convection regions of the North Atlantic Ocean are not regions where substantial vertical mass transport occurs. Instead, in line with geostrophic theory and idealized model simulations, also in these complex simulations sinking occurs in a narrow region adjacent to the continental boundary. Substantial sinking can only occur in regions where friction is an important factor in the vorticity balance (section 1), and hence this sinking region is much wider in the coarse and viscous ORCA1 simulation than in ORCA025. Nevertheless, for both simulations the width of the sinking region coincides with the location of the boundary current of the subpolar gyre. Note that this study focuses on the downward transport associated with the AMOC, not on dense water formation itself or on the properties of the waters that are transported downward. Considering the characteristics of deep ocean waters in models and observations, it is obvious that a connection has to exist between dense water formation by deep ocean convection and sinking. This study emphasizes that this connection has to be indirect, as the two processes occur at different locations.

In ORCA025, the amount of near-boundary sinking is controlled by alongshore density changes, except in the vicinity of overflows. There is a surprisingly good quantitative match with the theoretical relation derived by Spall and Pickart (2001), considering the complexity of the model analyzed here versus the simplifications made in deriving this relation. In ORCA1, the physical processes governing the sinking

downstream of Denmark Strait are not in agreement with these earlier results. There are several processes that may play a role here. First, the contribution of the overflows to the downwelling limb of the AMOC is larger in this simulation than in ORCA025: the transports in Denmark Strait and over the Iceland-Scotland Ridge already constitute 8.7 Sv of 17.3 Sv = 50% of the total sinking, while in ORCA025 this is 4.8 Sv of 13.3 Sv = 36% (Table 2). The vertical velocities associated with these overflows appear ill-represented in the ORCA1 model simulation (Figure 2). Overflows obviously affect the alongshore density gradient, and the same holds for the buoyant shelf waters that enter the deeper parts of the North Atlantic Ocean. The latter clearly affect the density over a much deeper part of the water column in ORCA1 than in ORCA25 (Figure 8b). An assumption made by Spall and Pickart (2001) in deriving equation (1) is that a balance arises between cooling of the boundary current and the alongshore advection of density. That is, the cross-shore density advection is assumed negligible. In the coarse resolution model ORCA1, this assumption may be violated near Davis Strait. There, probably as a consequence of the viscous nature of the flow, the flow does not follow the depth contours of the basin, and the cross-shore density advection may be nonnegligible.

It is at present unclear if the apparent poor representation of the processes governing the sinking in ORCA1 discussed in this paper is merely a peculiarity of this simulation or a more generic feature of low-resolution ocean models. This is an important issue to pursue: the century-long coupled climate model simulations that provide the basis for climate projections presented in, for example, the IPCC 5th Assessment Report typically have an ocean component with a 1° resolution (Cheng et al., 2013; Collins et al., 2013; Danabasoglu et al., 2014). While ocean-only simulations at higher resolution become more and more common, only a very limited number of the long-term climate model simulations planned in preparation of the IPCC 6th Assessment Report will have a resolution of 1/4° or less in the ocean (Haarsma et al., 2016). This implies that for the near future, the bulk of the long-term AMOC projections will still be based on climate model simulations with a low-resolution ocean component. If the dynamics of the sinking of dense waters in this type of models is poorly resolved, their response to changes in climate (e.g., their sensitivity to fresh water forcing at the surface) may also be affected. This implies that we need to evaluate the projections of future AMOC changes provided with these models with care.

References

Adcroft, A., Hill, C., & Marshall, J. (1997). Representation of topography by shaved cells in a height coordinate ocean model. *Monthly Weather Review*, *125*(9), 2293–2315.

Barnier, B., Madec, G., Penduff, T., Molines, J.-M., Treguier, A.-M., Sommer, J., et al. (2006). Impact of partial steps and momentum advection schemes in a global ocean circulation model at eddy-permitting resolution. *Ocean Dynamics*, *56*(5–6), 543–567. https://doi.org/10.1007/s10236-006-0082-1

Blanke, B., & Delecluse, P. (1993). Variability of the tropical Atlantic Ocean simulated by a general circulation model with two different mixed-layer physics. *Journal of Physical Oceanography*, *23*(7), 1363–1388.

Broecker, W. S. (1991). The great ocean conveyor. *Oceanography*, *4*, 79–89.

Brüggemann, N., Katsman, C. A., & Dijkstra, H. A. (2017). On the vorticity dynamics of the downwelling branch of the AMOC. *CLIVAR Exchanges Special Issue: CLIVAR Open Science Conference Award Winners*, *71*, 10–12.

Cenedese, C. (2012). Downwelling in basins subject to buoyancy loss. *Journal of Physical Oceanography*, *42*, 1817–1833. https://doi.org/10.1175/JPO-D-11-0114.1

Cheng, W., Chiang, J. C., & Zhang, D. (2013). Atlantic meridional overturning circulation (AMOC) in CMIP5 models: RCP and historical simulations. *Journal of Climate*, *26*(18), 7187–7197.

Collins, M., Knutti, R., Arblaster, J., Dufresne, J.-L., Fichefet, T., Friedlingstein, P., et al. (2013). *Long-term climate change: Projections, commitments and irreversibility* (pp. 1029–1136). Cambridge, UK: Cambridge University Press. https://doi.org/10.1017/CBO9781107415324.024

Danabasoglu, G., Yeager, S. G., Bailey, D., Behrens, E., Bentsen, M., Bi, D., et al. (2014). North Atlantic simulations in coordinated ocean-ice reference experiments phase ii (core-ii). Part i: Mean states. *Ocean Modelling*, *73*, 76–107.

Haarsma, R. J., Roberts, M. J., Vidale, P. L., Senior, C. A., Bellucci, A., Bao, Q., et al. (2016). High resolution model intercomparison project (HighResMIP v1.0) for CMIP6. *Geoscientific Model Development*, *9*, 4185–4208. https://doi.org/10.5194/gmd-9-4185-2016

Holte, J., & Straneo, F. (2017). Seasonal overturning of the Labrador Sea as observed by Argo floats. *Journal of Physical Oceanography*, *47*(10), 2531–2543.

Large, W. G., & Yeager, S. G. (2004). *Diurnal to decadal global forcing for ocean and sea-ice models: The data sets and flux climatologies*. Boulder, CO: National Center for Atmospheric Research.

Levitus, S. (1998). *World Ocean Database. Vol. 1: Introduction* (346 p.). Washington, D.C: U.S. Government Printing Office.

Marshall, J., & Schott, F. (1999). Open ocean deep convection: Observations, models and theory. *Reviews of Geophysics*, *37*, 1–64.

Pedlosky, J. (2003). Thermally driven circulations in small oceanic basins. *Journal of Physical Oceanography*, *33*, 2333–2340.

Pedlosky, J., & Spall, M. A. (2005). Boundary Intensification of Vertical Velocity in a β-plane basin. *Journal of Physical Oceanography*, *35*, 2487–2500.

Penduff, T., Juza, M., Brodeau, L., Smith, G. C., Barnier, B., Molines, J.-M., et al. (2010). Impact of global ocean model resolution on sea-level variability with emphasis on interannual time scales. *Ocean Science*, *6*(1), 269–284. https://doi.org/10.5194/os-6-269-2010

Pickart, R. S., & Spall, M. A. (2007). Impact of Labrador Sea convection on the North Atlantic meridional overturning circulation. *Journal of Physical Oceanography*, *37*, 2207–2227.

Rhines, P. B. (1986). Vorticity dynamics of the oceanic general circulation. *Annual Review of Fluid Mechanics*, *18*(1), 433–497.

Schott, F., & Stommel, H. (1978). Beta spirals and absolute velocities in different oceans. *Deep Sea Research*, *25*(11), 961–1010. https://doi.org/10.1016/0146-6291(78)90583-0

Scott, J. R., & Marotzke, J. (2002). The location of diapycnal mixing and the meridional overturning circulation. *Journal of Physical Oceanography*, *32*(12), 3578–3595.

Send, U., & Marshall, J. (1995). Integral effects of deep convection. *Journal of Physical Oceanography*, *25*, 855–872.

Spall, M. A. (2004). Boundary currents and water mass transformation in marginal seas. *Journal of Physical Oceanography*, *34*, 1197–1213.

Spall, M. A. (2008). Buoyancy-forced downwelling in boundary currents. *Journal of Physical Oceanography*, *38*(12), 2704–2721.

Spall, M. A. (2010). Dynamics of downwelling in an eddy-resolving convective basin. *Journal of Physical Oceanography*, *40*(10), 2341–2347.

Spall, M. A. (2011). On the role of eddies and surface forcing in the heat transport and overturning circulation in marginal seas. *Journal of Climate*, *24*(18), 4844–4858.

Spall, M. A., & Pickart, R. S. (2001). Where does dense water sink? A subpolar gyre example. *Journal of Physical Oceanography*, *31*, 810–826.

Sterl, A., Bintanja, R., Brodeau, L., Gleeson, E., Koenigk, T., Schmith, T., et al. (2012). A look at the ocean in the EC-Earth climate model. *Climate Dynamics*, *39*(11), 2631–2657.

Straneo, F. (2006). On the connection between dense water formation, overturning, and poleward heat transport in a convective basin. *Journal of Physical Oceanography*, *36*, 1822–1840. https://doi.org/10.1175/JPO2932.1

Timmermann, R., Goosse, H., Madec, G., Fichefet, T., Ethe, C., & Duliere, V. (2005). On the representation of high latitude processes in the ORCA-LIM global coupled sea ice–ocean model. *Ocean Modelling*, *8*(1), 175–201.

Uppala, S., Kallberg, P., Simmons, A., Andrae, U., da Costa Bechtold, V., Fiorino, M., et al. (2005). The ERA-40 re-analysis. *Quarterly Journal of the Royal Meteorological Society*, *131*, 2961–3012.

Wang, C., Zhang, L., Lee, S.-K., Wu, L., & Mechoso, C. R. (2014). A global perspective on CMIP5 climate model biases. *Nature Climate Change*, *4*(3), 201–205.

Winton, M., Hallberg, R., & Gnanadesikan, A. (1998). Simulation of density-driven frictional downslope flow in z-coordinate ocean models. *Journal of Physical Oceanography*, *28*(11), 2163–2174.